

Enhancing intensity and refractive index sensing capability with infrared plasmonic perfect absorbers

Fei Cheng,¹ Xiaodong Yang,^{1,2} and Jie Gao^{1,*}

¹Department of Mechanical and Aerospace Engineering, Missouri University of Science and Technology, Rolla, Missouri 65409, USA

²e-mail: yangxia@mst.edu

*Corresponding author: gaojie@mst.edu

Received April 2, 2014; revised April 21, 2014; accepted April 22, 2014;
posted April 23, 2014 (Doc. ID 209398); published May 23, 2014

An infrared refractive index sensor based on plasmonic perfect absorbers for glucose concentration sensing is experimentally demonstrated. Utilizing substantial absorption contrast between a perfect absorber (~98% at normal incidence) and a non-perfect absorber upon the refractive index change, a maximum value of figure of merit (FOM*) about 55 and a bulk wavelength sensitivity about 590 nm/RIU are achieved. The demonstrated sensing platform provides great potential in improving the performance of plasmonic refractive index sensors and developing future surface enhanced infrared spectroscopy. © 2014 Optical Society of America

OCIS codes: (160.3918) Metamaterials; (300.6340) Spectroscopy, infrared; (280.4788) Optical sensing and sensors.
<http://dx.doi.org/10.1364/OL.39.003185>

Metamaterials are artificially structured composites designed to create extraordinary electromagnetic properties that are not achievable in natural materials, such as negative refraction [1], invisible cloaking [2], near-zero permittivity [3], and indefinite cavities [4]. These intriguing phenomena can be tailored flexibly by designing artificial “meta-atoms,” including subwavelength plasmonic nanostructures supporting the excitation of propagating or localized surface plasmon resonances (LSPRs). Since LSPRs can couple light strongly with metamaterials and greatly enhance the light-matter interactions, plasmonic nanostructures enable many fascinating applications such as surface enhanced spectroscopy, photovoltaic solar cells, imaging, and biochemical sensing [5]. Different kinds of plasmonic nanostructures, such as nanoparticles with various shapes [6] and complex coupled plasmonic systems [7], have been employed in refractive index sensing and molecular vibration detection.

Typically, plasmonic nanostructures and metal-based metamaterials are subject to undesirable absorption loss because of the inevitable ohmic loss in metals. However, the absorption loss in plasmonic nanostructures and metamaterials can also be utilized to achieve perfect light absorption. First demonstrated in microwave [8] and terahertz [9] frequencies, metamaterial and plasmonic absorbers working at higher frequencies from visible [10] to infrared [11–13] regime have shown great promise in light harvesting and thermal detection. Recently, plasmonic perfect absorbers consisting of metal-dielectric-metal triple layers have been identified as a new type of LSPR sensors [5] and have attracted considerable interests in high-performance sensing [14–16]. The impedance matched optical resonance in plasmonic perfect absorbers can increase substantially the absorption contrast with that of a non-perfect one because of the change of the surrounding medium and therefore can enhance the refractive index sensing capability. In this Letter, we present a narrow-band, polarization-insensitive infrared refractive index sensor based on plasmonic perfect

absorbers for glucose concentration sensing. Both a large figure of merit and a high value of bulk wavelength sensitivity are demonstrated in experiments for the proposed structures.

Figure 1(a) illustrates the schematic of plasmonic perfect absorbers consisting of three functional layers, including the top 30 nm gold film and the bottom 150 nm gold mirror, which are separated by a 30 nm magnesium fluoride (MgF₂) dielectric spacer. Each layer was deposited with the electron-beam evaporation system at the rate of 0.2 Å/s on a glass substrate. A cross-shaped aperture array was then milled in the top gold layer with a focused ion beam system, with the dimensions of period $P = 550$ nm, aperture length $l = 490$ nm, and aperture width $w = 100$ nm. Figure 1(b) shows the scanning electron microscope image of the top view of the fabricated plasmonic perfect absorber. The optical response of the perfect absorber was calculated with a finite integration technique solver. Here the permittivity of bulk gold in the near-infrared is described by the Drude model $\epsilon_{\text{Au}} = \epsilon_{\infty} - \omega_p^2 / (\omega^2 + i\omega\gamma_p)$, where the background dielectric constant $\epsilon_{\infty} = 1$, the plasma frequency $\omega_p = 1.37 \times 10^{16}$ rad/s, and the damping constant $\gamma_p = 4.08 \times 10^{13}$ rad/s. Because of the surface scattering and grain boundary effects in thin films, the damping constant of the gold film in reality will be higher than

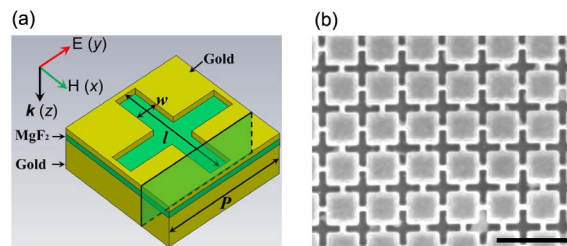


Fig. 1. (a) Schematic of one unit cell of the designed perfect absorber metamaterial and the incident light polarization configuration. (b) A SEM image of the fabricated perfect absorber metamaterial lattice (Top view). (Scale bar, 1 μm).

that of bulk gold [17] and was set to be three times that of bulk gold in the simulation in order to match the experimental results.

In order to characterize the optical properties of the fabricated plasmonic perfect absorber, the optical reflection spectra were measured with a Fourier transform infrared spectrometer (Nicolet 6700). The reflectance (R) spectrum was obtained by dividing the reflection intensity of our sample by that of a silver coated mirror, and the absorbance (A) spectrum was then obtained from $A = 1 - R$, since the transmittance is totally eliminated by the bottom gold mirror. Figures 2(a) and 2(b) show the measured reflectance and absorbance spectra at normal incidence, with air and water on the sample surface, respectively. The spectrum shift because of the refractive index change from air to water demonstrates the feasibility of the perfect absorber working as a refractive index sensor. As characterized by the black solid curve shown in Fig. 2(a), a near-zero reflectance ($R = 2.3\%$), corresponding to a high absorbance $A = 97.7\%$ as shown in Fig. 2(b) can be obtained at 141.2 THz (impedance matched frequency f_0) with air ($n = 1$) being the surrounding medium. However, a significant increase of the reflectance intensity from 2.3% to 36.4% at this frequency is observed when water ($n = 1.312$, red solid curve) is applied on the sample surface. Therefore, the proposed plasmonic perfect absorber provides a high reflection contrast between surrounding media with different refractive indices and thus can serve as a promising platform for detecting solutions with different concentrations with high sensitivity. Figures 2(c) and 2(d) show the numerical simulation results of reflectance and absorbance spectra with air or water being the surrounding medium. The calculated reflectance minimum increases from 1.2% (black dashed curve) to 46.2% (red dashed curve) at 142.3 THz, showing good agreement with the experimental results.

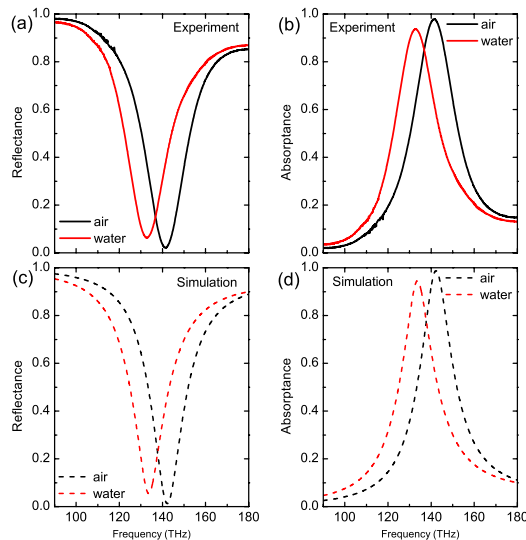


Fig. 2. FTIR measured (a) reflectance and (b) absorbance spectra by changing the adjacent dielectric medium from air (black solid) to water (red solid) at normal incidence. The corresponding numerical simulated (c) reflectance and (d) absorbance spectra in air (black dashed curve) and water (red dashed curve).

The sensing capability of the plasmonic perfect absorber can be examined by evaluating the figure of merit which is typically defined as $FOM = S/\text{FWHM}$, where S represents the bulk wavelength sensitivity (denoted as $\Delta\lambda/\text{RIU}$) and FWHM is the full-width bandwidth at half maximum. This definition allows plasmonic nanostructures to be judged against one another as sensing platforms independent of shape and size [18]. Alternatively, a relative intensity change dI/I of the resonance spectrum at a fixed wavelength λ_0 because of a small index change dn can also be detected, especially in the situation where the plasmonic resonance does not follow a simple Lorentzian peak. Therefore, an alternative figure of merit can be defined as $FOM^* = (dI(\lambda)/dn(\lambda))/I(\lambda)$, where $I(\lambda)$ is the intensity in air and $dI(\lambda)$ is the intensity change induced by the refractive index change dn . According to this definition, a sharp reflectance dip with narrow linewidth is as crucial as a small reflection intensity, and the maximum value of FOM^* can be obtained around the perfect absorption frequency [5]. Figure 3(a) shows the experimental result of FOM^* (red dashed curve) in water ($dn = 0.312$) as a function of frequency. The maximum value of the measured FOM^* is about 55, and it occurs nearly at the position of perfect absorbance in air. Figure 3(b) shows the corresponding numerical simulation results. Since the reflectance at perfect absorption frequency of the calculated spectrum (black solid curve) is half that of the experimental curve, the simulation result of FOM^* is about twice that of the experimental value. Notably, the FOM^* of the plasmonic perfect absorber platform is much higher than that of conventional LSPR-based sensing platforms such as the plasmonic gold nanorods [19], benefiting from the fact that a great contrast between the reflectance from a perfect absorber and that from a non-perfect one can be obtained with a small index change.

Furthermore, in order to determine the sensitivity of the plasmonic perfect absorber as a refractive index sensor, the reflectance spectra are measured in aqueous glucose solutions (Sigma-Aldrich) with different concentrations varying from 0% to 45% (weight ratio). As depicted in Fig. 4(a), the resonant frequency of the plasmonic perfect absorber is highly dependent on the dielectric constant of the surrounding medium, where the measured reflectance spectrum is shifted to lower frequencies as the concentration of glucose solution is increased. The reflectance resonance redshifts from 132.8 THz in water ($n = 1.312$) to 130.3 THz in 45%

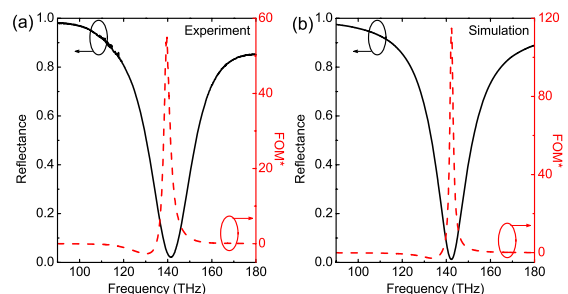


Fig. 3. (a) Experimental and (b) simulated FOM^* (red dashed curve) as a function of frequency. The black solid curve in each figure shows the reflectance spectrum measured in air.

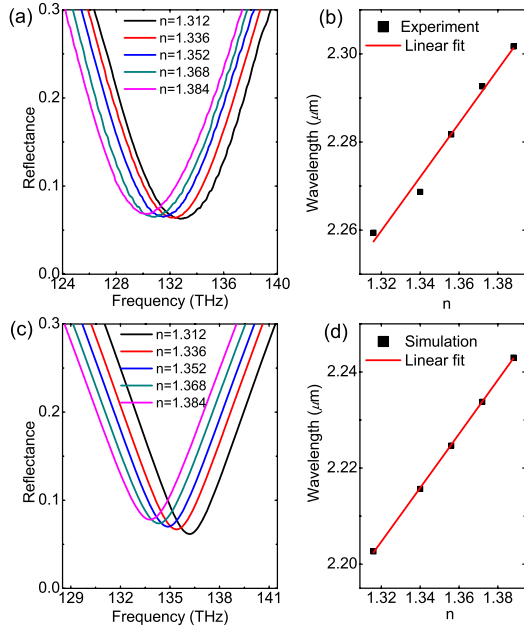


Fig. 4. (a) Measured and (c) simulated reflectance spectra tuning for the sample by changing the surrounding medium from water to 45% aqueous glucose solution. Linear fit (red curves) of the (b) measured and (d) simulated resonance wavelengths (black squares) as a function of refractive index of the surrounding medium. The slope of the fitting curve in each figure depicts the bulk wavelength sensitivities.

glucose solution ($n = 1.384$). According to the linear fitting of the resonant frequencies (black squares in Fig. 4(b)), the experimentally determined bulk wavelength sensitivity is about 590 nm/RIU. This result is remarkable when compared with most plasmonic nanostructure-based sensors and planar metamaterial LSPR sensors [20]. Figures 4(c) and 4(d) present the numerical simulated spectral shift of the plasmonic perfect absorber, and the simulation results match well with the experimental data.

To reveal the physical mechanism of perfect light absorption in the plasmonic perfect absorber, the electromagnetic field distributions at the resonant frequency are investigated numerically. Figure 5(a) illustrates the magnetic field (contour plot, $|\vec{H}|$) and current density (arrows, \vec{J}) distributions in the y - z cutting plane (80 nm from the aperture center) as depicted in Fig. 1(a). It is shown that antiparallel currents are excited in the top gold film and the bottom gold mirror, forming a magnetic resonance because of the fact that the circulating currents can result in a magnetic moment which can strongly interact with the magnetic field of the incident light [5,12,21]. At the resonant frequency, a significantly enhanced magnetic field can be established and well confined in the intermediate dielectric spacer, as depicted by the contour plot in Fig. 5(a). Figure 5(b) shows the electric field (contour plot, $|\vec{E}|$) and polarization (arrows, \vec{P}) distributions at the resonant frequency. Unlike the magnetic field, the electric field concentrates mostly on the bottom edge of the top gold layer. The divergence and convergence of the electric field (denoted by \vec{P}) at the left and right corners of the cross-shaped aperture imply the accumulation of polarized positive and

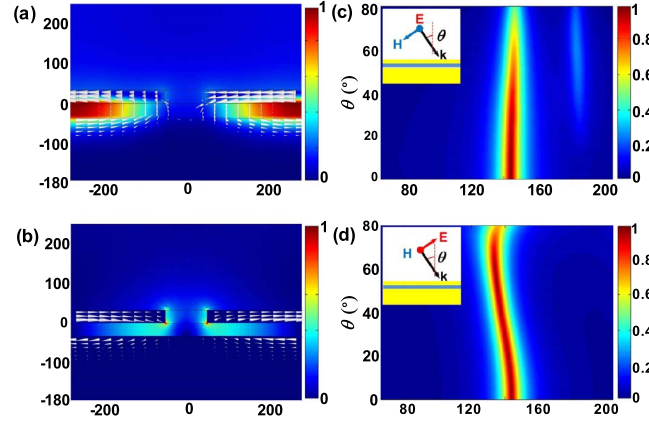


Fig. 5. (a) Magnetic field (contour plot, $|\vec{H}|$) and current density (arrows, \vec{J}) distributions on the y - z cutting plane depicted in Fig. 1(a). (b) The electric field (contour plot, $|\vec{E}|$) and polarization (arrows, \vec{P}) distributions in the cutting plane. The simulated absorbance bands as functions of frequencies and incident angles for TE (c) and TM (d) polarization.

negative charges, which demonstrates a strong electric dipole resonance [22]. The coexistence of electric dipole and magnetic dipole resonance in the plasmonic perfect absorber can result in matched impedance to the free space, leading to negligible reflection, i.e., perfect absorption of incoming light. Here we employ the electric and magnetic resonance assisted impedance matching to explain qualitatively the observed phenomena in our structures. Alternatively, several other theoretical methods have been proposed for quantitative interpretation of underlying mechanisms of perfect absorption, including the multiple reflections interference theory [23–26], the equivalent circuit model [27–29], and the grating theory [30]. These theoretical methods provide valuable guidance in the design and analysis of metamaterial perfect absorbers, as well as new perspectives in exploring potential applications.

Numerical simulations show that the plasmonic perfect absorber works for a wide range of incident angles, and the absorption resonance remains strong even at large incident angles under appropriate polarization. Figures 5(c) and 5(d) show the simulated absorbencies as functions of frequency and the angle of incidence for both transverse electric (TE) and transverse magnetic (TM) polarization, with the incident field configurations shown in figure insets. As illustrated in Fig. 5(c), the absorption intensity under TE polarization gradually decreases as the incident angle (θ) increases. For this polarization, the smaller horizontal magnetic field component at larger incident angles cannot drive the circulating currents efficiently [9] so that the maximum absorbance gets weaker. Meanwhile, the resonant frequency remains almost the same, i.e., the absorbance band is almost angle insensitive. However, as shown in Fig. 5(d), for TM polarization, the absorbance band slightly shifts to lower frequencies with the increased incident angles because of weak surface wave coupling between neighboring resonators (cross-apertures) [31]. The absorption intensity remains above 70% with the incident angle up to $\theta = 80^\circ$. The all-angle high absorption is because of the fact that the magnetic field component

of incident light remains unchanged at various incident angles for TM polarization, so that the magnetic dipole resonance can always be excited well. These results indicate that the plasmonic perfect absorber sensors can maintain high sensing performance at a wide range of incident angles, especially for TM polarization.

In conclusion, a polarization-insensitive, infrared refractive index sensor based on plasmonic perfect absorbers has been experimentally demonstrated. Because of the impedance matched optical resonance, the plasmonic perfect absorber provides enhanced infrared absorption contrast and thus high figure of merit with the refractive index change of surrounding media. With the demonstrated sensing capability of glucose concentration, the perfect absorber metamaterial also can be used in bio-medical sensing where perfect absorbance resonances match the molecular vibrational fingerprints. Furthermore, the current sensor design is highly scalable and can be tuned to the visible or gigahertz frequency regimes.

This work is supported by ERDC and MRC at Missouri S&T, the University of Missouri Research Board and Interdisciplinary Intercampus Research Program.

References

1. R. A. Shelby, D. R. Smith, and S. Schultz, *Science* **292**, 77 (2001).
2. J. B. Pendry, D. Schurig, and D. R. Smith, *Science* **312**, 1780 (2006).
3. A. Alù, M. G. Silveirinha, A. Salandrino, and N. Engheta, *Phys. Rev. B* **75**, 155410 (2007).
4. X. Yang, J. Yao, J. Rho, X. Yin, and X. Zhang, *Nat. Photonics* **6**, 450 (2012).
5. N. Liu, M. Mesch, T. Weiss, M. Hentschel, and H. Giessen, *Nano Lett.* **10**, 2342 (2010).
6. S. Lal, S. Link, and N. J. Halas, *Nat. Photonics* **1**, 641 (2007).
7. W. Chihhui, B. K. Alexander, A. Ronen, A. Nihal, Y. Ahmet Ali, A. Hatice, and S. Gennady, *Nat. Mater.* **11**, 69 (2011).
8. N. I. Landy, S. Sajuyigbe, J. J. Mock, D. R. Smith, and W. J. Padilla, *Phys. Rev. Lett.* **100**, 207402 (2008).
9. H. Tao, C. M. Bingham, A. C. Strikwerda, D. Pilon, D. Shrekenhamer, N. I. Landy, K. Fan, X. Zhang, W. J. Padilla, and R. D. Averitt, *Phys. Rev. B* **78**, 241103 (2008).
10. Z. Fang, Y.-R. Zhen, L. Fan, X. Zhu, and P. Nordlander, *Phys. Rev. B* **85**, 245401 (2012).
11. X. Liu, T. Starr, A. F. Starr, and W. J. Padilla, *Phys. Rev. Lett.* **104**, 207403 (2010).
12. J. Hao, J. Wang, X. Liu, W. J. Padilla, L. Zhou, and M. Qiu, *Appl. Phys. Lett.* **96**, 251104 (2010).
13. C. Wu, B. Neuner, G. Shvets, J. John, A. Milder, B. Zollars, and S. Savoy, *Phys. Rev. B* **84**, 075102 (2011).
14. A. Tittl, P. Mai, R. Taubert, D. Dregely, N. Liu, and H. Giessen, *Nano Lett.* **11**, 4366 (2011).
15. K. Chen, R. Adato, and H. Altug, *ACS Nano* **6**, 7998 (2012).
16. L. Yongqian, S. Lei, S. Chen, Y. Chunmeng, D. Jinjun, and F. Yu, *Sci. Rep.* **3**, 2865 (2013).
17. S. Zhang, W. Fan, K. J. Malloy, S. R. J. Brueck, N. C. Panou, and R. M. Osgood, *J. Opt. Soc. Am. B* **23**, 434 (2006).
18. L. J. Sherry, S.-H. Chang, G. C. Schatz, R. P. Van Duyne, B. J. Wiley, and Y. Xia, *Nano Lett.* **5**, 2034 (2005).
19. J. Becker, A. Trgler, A. Jakab, U. Hohenester, and C. Snnichsen, *Plasmonics* **5**, 161 (2010).
20. N. Liu, T. Weiss, M. Mesch, L. Langguth, U. Eigenthaler, M. Hirscher, C. Snnichsen, and H. Giessen, *Nano Lett.* **10**, 1103 (2010).
21. W. Cai, U. K. Chettiar, H.-K. Yuan, V. C. de Silva, A. V. Kildishev, V. P. Drachev, and V. M. Shalae, *Opt. Express* **15**, 3333 (2007).
22. Y. He, H. Deng, X. Jiao, S. He, J. Gao, and X. Yang, *Opt. Lett.* **38**, 1179 (2013).
23. J. Zhou, H.-T. Chen, T. Koschny, A. K. Azad, A. J. Taylor, C. M. Soukoulis, and J. F. O'Hara, <http://arxiv.org/abs/1111.0343>.
24. H.-T. Chen, *Opt. Express* **20**, 7165 (2012).
25. X. Shen, Y. Yang, Y. Zang, J. Gu, J. Han, W. Zhang, and T. Jun Cui, *Appl. Phys. Lett.* **101**, 154102 (2012).
26. T. Wanghuang, W. Chen, Y. Huang, and G. Wen, *AIP Adv.* **3**, 102118 (2013).
27. C. Wu and G. Shvets, *Opt. Lett.* **37**, 308 (2012).
28. M. Pu, C. Hu, M. Wang, C. Huang, Z. Zhao, C. Wang, Q. Feng, and X. Luo, *Opt. Express* **19**, 17413 (2011).
29. M. P. Hokmabadi, D. S. Wilbert, P. Kung, and S. M. Kim, *Opt. Express* **21**, 16455 (2013).
30. Y. Zeng, H.-T. Chen, and D. A. R. Dalvit, *Opt. Express* **21**, 3540 (2013).
31. D. Y. Shchegolkov, A. K. Azad, J. F. O'Hara, and E. I. Simakov, *Phys. Rev. B* **82**, 205117 (2010).